Journal of Sound and Vibration (1997) **200**(2), 195–225

ACOUSTIC MODELLING OF MULTIPLE PATH SILENCERS WITH EXPERIMENTAL VALIDATIONS

P. O. A. L. Davies, M. F. Harrison and H. J. Collins†

Institute of Sound and Vibration Research, University of Southampton, Southampton SO17 1BJ, England

(*Received* 5 *March* 1996, *and in final form* 2 *August* 1996)

The results are presented of an investigation to identify and quantify the relative influence of their geometrical features with that of other relevant physical and operational factors on the acoustic behaviour of cross-flow silencers. This was accomplished by comparing the measured with the predicted attenuation performance of a sequence of generic examples of cross-flow and flow-reversing silencing elements. Such silencers are all assembled around a common geometric central feature, consisting of an expansion chamber spanned by the perforated inlet and outlet pipes. The predictive modelling included the simplifying assumption that the wave motion throughout the central element is essentially one-dimensional and directed along the pipe and chamber axes, with radial propagation existing only through walls. The existence of any axial mean velocity gradients was also neglected, so that the mean flow velocity and all the other relevant physical properties of the acoustic medium were represented by their locally space averaged values. Comparisons between measured and predicted performance of some thirty representative models are summarized and discussed in terms of the relative significance of their relevant physical and operational features on their attenuation performance. The subsequent validation of the acoustic modelling included the identification of those features that required further investigation. Nevertheless, the results demonstrate that the predictive modelling provides adequately realistic predictions of silencer acoustic performance for practical application to exhaust system design.

1. INTRODUCTION

Cross-flow and flow-reversing silencers form component elements of contemporary automotive exhaust systems, where relatively high acoustic performance is required from restricted spaces. A sequence of common generic types is illustrated schematically in Figure 1. In the figure they have been assembled in two groups, in accordance with the path taken through them by the exhaust flow and acoustic energy flux. However, it is clear from the figure that all the examples have a basic central geometrical arrangement in common, which consists of two perforated tubes spanning an expansion chamber. In the first group of three, the layout of plug and cross-flow silencers is described in Figures 1(a) and 1(b), respectively, while that of the cross-flow reversing one is described in Figure 1(bR). In this group, the exhaust flow is forced through the perforate as it travels from the inlet to the outlet pipe, while the acoustic energy travels along the same path.

With the second pair in Figures 1(c) and 1(d), one can see that the bulk of the exhaust gas normally flows along each pipe and is transferred from the inlet to the outlet pipe via

†Now at Ford Motor Company, Laindon, Basildon, Essex, SS15 6EE, U.K.

0022–460X/97/070195 + 31 $25.00/0/sv960716

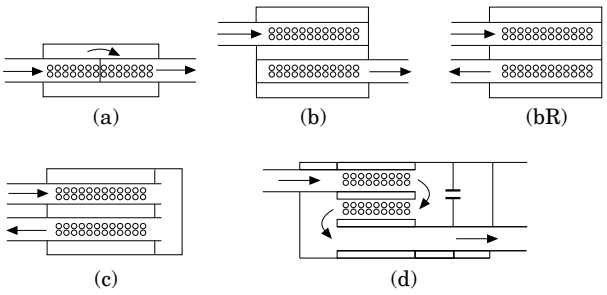

Figure 1. Silencer types. (a) Plug; (b) cross-flow; (bR) cross-flow reversing; (c) cross-flow reversing with parallel paths; (d) triflow with Helmholtz resonator.

a flow reversing expansion chamber. This structural arrangement now provides two parallel paths for the flow of gas and the transmission of acoustic energy. The triflow type in Figure 1(d) is particularly popular, since the gas enters and leaves the silencer in the same direction along the exhaust system. The example in Figure 1(c) normally constitutes a component of the triflow, and in consequence is seldom identified as a separate item. For convenience, it is identified here as a cross-flow with parallel paths. A Helmholtz resonator is sometimes added to the flow reversing chamber, to enhance the attenuation over specific narrow bands, so an example has been included in the triflow silencer in Figure 1(d).

Despite the wide adoption for practical application of the whole range of silencers illustrated in Figure 1, predictive models of their acoustic characteristics appear to have been confined to the first group of three in the figure. Furthermore, experimentally validated models are apparently available [1] only for the type defined in Figure 1(a). Clearly, when silencers of this group are incorporated in an exhaust system, a relatively strong mean velocity gradient must exist along the perforated pipes. This was accounted for in the predictive model described in reference [1] by adopting an axially distributed segmentation approach for the modelling. Later predictive models (see, for example, reference [2]), adopted a distributed parameter approach to develop the defining equations, but although they were included in the original formulation, the velocity gradient terms were omitted during the calculations, raising some doubts concerning the realism of the resulting predictions. A new solution [3] that retains the velocity gradients has now resolved this uncertainty, since it showed that their influence on the predicted transmission loss remains sufficiently small to be neglected for practical purposes.

This result justifies adoption of the simplifying assumption that the existence of any mean axial velocity gradients in the perforated pipes may be neglected in the development of predictive models of the silencers illustrated in Figure 1 for practical applications. With the exception of the plug muffler for which validated predictive models already exist [1], predictions of the acoustic performance of the remainder are compared with the results of measurements in what follows here. Although they were essentially similar to the predictive models adopted in references [1–3], there are differences in detail, mainly to ensure that practical realism in the predictive modelling [4] was maintained as far as possible. For example, provision for the presence of temperature and density gradients was included in modelling. In place of transmission loss, they now provide predictions of the relative changes in amplitude of the positively and negatively travelling component waves, represented respectively as p^+ and p^-, in pipes attached to the silencer's inlet and outlet ports, to facilitate comparisons with the measured behaviour.

Measurements of the corresponding component wave spectra were made in these two pipes, while the system was being excited by white noise for comparison with predictions by the new models. A dedicated four-channel digital data acquisition system was employed to acquire store and process signal records of appropriate length. This technique has been employed at Southampton as a well established experimental procedure [5] since the mid-1970s, and is described further in Appendix A. Performed initially with zero flow, the measurements were repeated with Mach numbers 0·05 and 0·1 in the silencer inlet pipe. Measurements at higher Mach numbers were found to be too strongly contaminated by flow generated noise, to provide realistic validations of the predicted acoustic behaviour, which currently does not include the generation of flow noise within the silencer elements.

2. THE PREDICTIVE MODELS

The models here predict the acoustic transfer across the silencers, illustrated schematically in Figures 1(b)–1(d). The model is derived by separating the overall transfer into a number of separate steps, beginning with transfers over the central section that extends only along the perforated lengths of the pipes and has already been identified as being common to all. Here there exists transfer from the inlet pipe to the chamber and from the central chamber to the outlet pipe as illustrated in Figure 2. It is convenient to divide this central section further into three corresponding regions which are coupled through the perforated walls. Acoustic propagation along each pipe and along the central chamber is assumed to be essentially one-dimensional, with radial propagation and gas flow between the regions existing only at the perforated walls.

2.1. THE WAVE EQUATIONS FOR THE CENTRAL SECTION

The appropriate equations expressing conservation of mass and momentum [4, 5] were combined to derive the three coupled wave equations describing the associated axial acoustic pressure distribution in each region. The existence of any angular variation of pressure around the circumferences of the pipes was neglected, although some observations [6] indicate that this might have limited validity in some instances. The two-dimensional expression describing the fluctuating acoustic pressure distribution in each region j is expressed by [5]

$$\left[(1 - M_j^2)\frac{\partial^2}{\partial x^2} - \frac{2M_j}{c_j}\frac{\partial^2}{\partial x\,\partial t} - \frac{1}{c_j^2}\frac{\partial}{\partial t^2}\right] p_j = \frac{\rho_j}{r}\frac{\partial}{\partial r}\frac{D}{Dt}(rv_j), \qquad j = 1,\ 2,\ 3, \qquad \text{(1a–c)}$$

where the right side describing the radial motion at the perforated walls can be interpreted as a forcing term, while D/Dt corresponds to $\partial/\partial t + M_j c_j\,\partial/\partial x$. Also, c_j, ρ_j and M_j are, respectively, the appropriate values of the local space averaged sound speed, mean density in the holes and Mach number of the mean axial flow, with v_j the similarly averaged radial

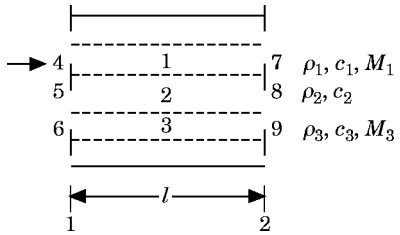

Figure 2. A central element with two perforated pipes.

particle velocity through the perforated wall. (See also the discussion of reference [3] in the *Journal of Sound and Vibration* **191**, 606–611.)

The corresponding one-dimensional expressions describing the acoustic pressure distribution in each region are derived by integrating equations (1) over the cross-section area S_j of the respective regions. This then yields

$$\left[(1-M_j^2)\frac{\partial^2}{\partial x^2}-\frac{2M_j}{c_j}\frac{\partial^2}{\partial x\,\partial t}-\frac{1}{c_j^2}\frac{\partial}{\partial t^2}\right]p_j=\frac{L_j}{S_j}\rho_j\frac{D}{Dt}v_j,\qquad j=1,\ 2,\ 3,\qquad \text{(2a–c)}$$

where L_j is the appropriate local value of the perforated wall perimeter. Within the pipes this is the corresponding inner perimeter, while in the expansion chamber this is the sum of their outer perimeters. One is reminded that, in equations (2a), (2b) and (2c) radial motion is restricted to the perforated walls, and also that in the expansion chamber external to the pipes $M_j = M_2 = 0$.

The particle velocities in equations (2) are eliminated by applying the mass continuity equation to the flow through the perforate. With fluid at rest on both sides, there will be continuity of particle velocity and v_j is simply equal to the ratio of the fluctuating pressure difference across the wall Δp_w to the perforated wall impedance Z_w. Empirically conditioned analytic expressions for Z_w were adopted from reference [5] and are summarized in Appendix B. With flow on one side of the wall, as is the case here, it has been argued that continuity of particle displacement would be more appropriate. But after a thorough investigation of both alternatives [5] it was found continuity of velocity yielded a predicted behaviour that remained in better agreement with observations. Subsequent to the appropriate substitutions for v_j in terms of p_j and Z_w, as with equations (2), the result will be linear in $p_j(x, t)$ with coefficients that are independent of x. For each of the three regions its Fourier transform giving the corresponding spectral density $p_j(x, \omega)$, with $k_j = \omega/c_j$ becomes, respectively,

$$[(1-M_1^2)\,\partial^2/\partial x^2 - M_1(2\mathrm{i}k_1+s_1)\,\partial/\partial x + (k_1^2-\mathrm{i}k_1 s_1)]p_1 = -[M_1 s_1\,\partial/\partial x + \mathrm{i}k_1 s_1]p_2, \quad \text{(3a)}$$

$$[\partial^2/\partial x^2 + k_2^2 - \mathrm{i}k(s_{12}+s_{23})]p_2 = -\mathrm{i}k_2(s_{12}p_1 + s_{23}p_2), \quad \text{(3b)}$$

$$[(1-M_3^2)\,\partial^2/\partial x^2 - M_3(2\mathrm{i}k_3+s_3)\,\partial/\partial x + (k_3^2-\mathrm{i}k_3 s_3)]p_3 = -[M_3 s_3\,\partial/\partial x + \mathrm{i}k_1 s_1]p_2, \quad \text{(3c)}$$

where p_1, p_2 and p_3 are, respectively, the spectral component acoustic pressures in the inlet pipe, or region 1, the expansion chamber, or region 2, and the outlet pipe, or region 3. Also

$$s_1=\frac{2}{a_1}\frac{\rho_1 c_1}{Z_{12}},\qquad s_{12}=\frac{2\pi(a_1+t_1)\rho_2 c_2}{S_2 Z_{12}}\qquad s_{23}=\frac{2\pi(a_3+t_3)}{S_2 Z_{23}}\rho_2 c_2,\qquad s_3=\frac{2}{a_3}\frac{\rho_3 c_3}{Z_{23}}, \quad \text{(4a–d)}$$

where a_1, t_1, Z_{12} and a_3, t_3, Z_{23} are respectively, the inside radius, wall thickness and impedance of the inlet and outlet pipes, while S_2 is the net cross-section area of the expansion chamber, after subtracting the areas occupied by the pipes.

As should be expected, equations (3) are essentially the same as those found elsewhere, for example, in references [1] and [2], but the gas and flow conditions are now represented by their space averaged values over each region of the central section of the silencer, as illustrated in Figure 2. Where relevant, due account must be included for any temperature and static pressure gradients present. As such, they do not yet provide a complete predictive model of the silencers illustrated in Figures 1(a)–1(d), but only of the coupled wave motion in the central section.

Equations (3) can be reduced to a sixth order equation, for example describing the distribution of fluctuating pressure p_2 in the expansion chamber, which can then be solved

to evaluate the corresponding six roots, or eigenvalues, λ_n. In some instances after the reduction, the values of the resulting complex coefficients may differ by two or three orders of magnitude. Even so, in contrast to some reports in the literature, for example reference [2], no difficulty was found in finding stable solutions for λ_n provided that sufficient numerical precision was available to minimize uncertainties arising from rounding errors in the calculations with the algorithm adopted for this purpose. Alternatively, a numerical decoupling of equations (3) [2], or a matrizant solution [3] of the corresponding six first order equations in p, ρcu and M, may be adopted instead. An investigation of the first two alternatives [6] showed that solutions of either the sixth order equation, or its numerically decoupled alternative, yielded closely similar values for λ_n.

These values can be substituted back into equations (3a), (3b) and (3c) to yield the following three expressions describing the pressure distributions $p_j(x, \omega)$ in the three regions in Figure 2: namely,

$$p_j(x, \omega) = \sum_{n=1}^{6} B_{jn} \exp(\lambda_n x), \qquad j = 1, 2, 3. \tag{5a}$$

Substitution for p_1 and p_2 from equations (5a) into equation (3a) shows that the pressure amplitudes B_{1n} and B_{2n} are related by

$$B_{1n} = \phi_{1n} B_{2n}, \tag{5b}$$

where

$$\phi_{1n} = -s_1(M_1\lambda_n + \mathrm{i}k_1)/[(1 - M^2)\lambda_n^2 - M_1(s_1 + 2\mathrm{i}k_1)\lambda_n + (k_1^2 - \mathrm{i}k_1 s_1)]. \tag{5c}$$

Also substituting for p_2 and p_3 in equation (3c) shows that B_{3n} and B_{2n} are related by

$$B_{3n} = \phi_{3n} B_{2n}, \tag{5d}$$

where ϕ_{3n} is the result of substituting the subscript 3 for the subscript 1 in equation (5c). These expressions demonstrate that the pressure distributions differ distinctly in the three regions, but equations (5b) and (5d) represent the relations between them.

The values of the corresponding six B_{2n} pressure amplitudes are determined first by establishing the six boundary conditions evaluated over plane 1 and plane 2 at the positions that are labelled 4–9 in Figure 2. Clearly, across each transfer plane, there must be continuity of acoustic pressure and of particle velocity, together with conservation of momentum. One should note that in the special case of zero flow in the absence of temperature gradients and with two perforated tubes of identical geometry, equations (5) become degenerate and there are then only four distinct roots, with corresponding changes to the necessary boundary conditions.

2.1.1. *Conservation of momentum*

Following established practice [4], acoustic conditions in the silencer input and output pipes are normally expressed in terms of the local amplitudes p^+ and p^-, respectively, of the positively and negatively travelling component waves. With plane wave motion the corresponding acoustic pressure p and particle velocity u, are expressed in terms of the component wave amplitudes by

$$p = p^+ + p^- \qquad \text{and} \qquad \rho cu = p^+ - p^-, \tag{6a,b}$$

which provide useful alternatives for describing acoustic pressure and velocity. The ratio $p/\rho cu$, or $(p^+ + p^-)/(p^+ - p^-)$ defines the dimensionless impedance ζ.

With one-dimensional flow, conservation of momentum is expressed by

$$(\partial/\partial t + Mc\,\partial/\partial x)u + (1/\rho)\,\partial p/\partial x = 0, \tag{7a}$$

which, with the substitution of $B_n \exp(\lambda_n x) \exp(\mathrm{i}\omega t)$ for p, and p/ζ for $\rho c u$, becomes

$$[\lambda_n(\zeta + M) + \mathrm{i}k]B_n \exp(\lambda_n x) = 0, \tag{7b}$$

where the unknown values include the value of dimensionless impedance ζ as well as those of B_n.

Alternatively, with $u = (p^+ - p^-)/\rho c$ for the second substitution, equation (7a) becomes.

$$B_n\lambda_n \exp(\lambda_n x)/(M\lambda_n + \mathrm{i}k) + (p^+ - p^-) = 0. \tag{7c}$$

Specifically, across the inlet plane at position 4 in Figure 2, conservation of momentum between inlet pipe and region 1 is expressed by

$$B_{1n}\psi_{1n} = (p_4^+ - p_4^-)/\rho_4 c_4, \tag{7d}$$

where

$$\psi_{1n} = -\lambda_n \exp(\lambda_n x)/(M_1\lambda_1 + \mathrm{i}k)\rho_1 c_1. \tag{7e}$$

Similarly, across the outlet plane at position 9, it is expressed by

$$B_{3n}\psi_{3n} = (p_9^+ - p_9^-)/\rho_9 c_9, \tag{7f}$$

where ψ_{3n} is defined by equation (7e) with the subscript 1 replaced by 3.

2.2. THE BOUNDARY CONDITIONS IN THE CENTRAL SECTION

To establish the values of the six fluctuating pressure amplitudes B_{2n} in equation (5a), one needs six boundary conditions. These, in general must satisfy continuity of pressure and velocity, or conservation of momentum at the designated transfer planes. Combining Figure 2 with Figure 1 produces the result in Figure 3, which presents all the information necessary to identify and evaluate the required conditions. Following established practice [4], the acoustic transfer along the tailpipe is calculated first, starting at its termination. This provides the component wave amplitudes p_{in}^+ and p_{in}^- at the inlet plane of the tailpipe. This is the plane between region 3 and position 9 in Figure 3(a) or, alternatively, between

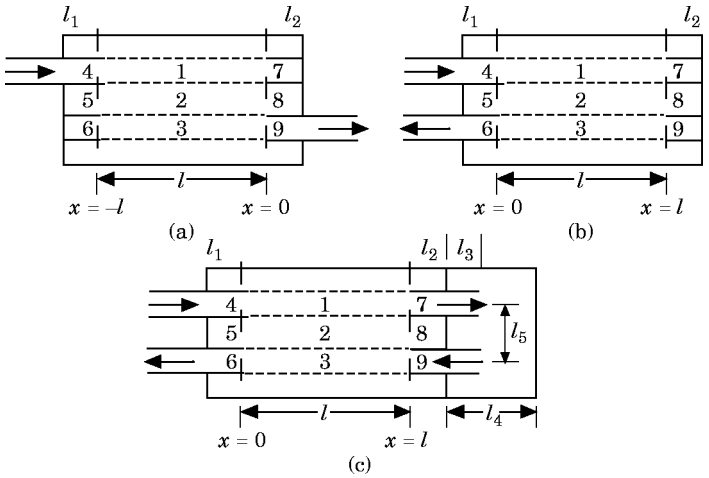

Figure 3. Silencer geometries. (a) Cross-flow silencer; (b) cross-flow reversing; (c) flow-reversing chamber.

region 3 and position 6 in Figures 3(b) and 3(c). Since the pressure must be continuous across the transfer plane one of either $p_9^+ + p_9^-$ or $p_6^+ + p_6^-$ is equal to $p_{in}^+ + p_{in}^-$, which gives one boundary condition. Equation (7f) provides a second.

Referring to Figure 3, one sees that the remaining four boundary conditions that are still required can be specified by satisfying conservation of momentum expressed by equation (7b) at the relevant interfaces. These are between region 1 and position 7, between region 2 and positions 5 and 8, and between region 3 and one of either positions 6 or 9. However, one must first establish the values of the corresponding dimensionless impedances ζ_j, $j = 5, \ldots, 9$, so these can then be substituted in equation (7b).

2.2.1. *The reflection coefficients and impedances*

The dimensionless impedance $\zeta = (p^+ + p^-)/(p^+ - p^-)$ is readily evaluated in terms of the pressure reflection coefficient r, defined as the ratio of negative to positive component wave amplitudes, p^-/p^+, and ζ is then equal to $(1 + r)/(1 - r)$. In Figure 3(a), r_7 and r_8 on the right side are both equal to $r_w \exp(-2ikl_2)$ as demonstrated in reference [4], where r_w is the reflection coefficient at the wall on the right side. However, on the left side of the central element, r_5 and r_6 are both equal to $\exp(2ikl_1)/r_w$), since r_w is normally still expressed as the ratio of reflected to incident wave amplitude at the wall. The same expressions apply to r_7, r_8 and r_9 on the right side and to r_5 on the left in Figure 3(b). Similarly, they apply respectively to r_8 and to r_5 in Figure 3(c).

In Figure 3(c) the reflection coefficients r_7 and r_9, however, must be calculated with due account taken of the reactive behaviour of the attached flow-reversing chamber. This has a chamber length l_4 with the two pipes with centres a distance l_5 apart, protruding a distance l_3 into it. Experimental evidence indicates that a one-dimensional predictive model yielding a first approximation to the acoustic behaviour is obtained by subtracting the mean diameter of the two pipes from l_5 and adding the result to the sum of $l_2 + l_3$ to give the effective length of the inlet pipe. That for the outlet pipe is simply $l_2 + l_3$. Presumably, this addition to the inlet pipe makes some appropriate adjustment or end correction for the time taken for waves to travel between the inlet and outlet pipes across the expansion. Appropriate procedures for the calculation of r_7 and r_9 in Figure 3(c) are described in reference [4]. They include the influence on wave propagation of mean flow and that of the evanescent waves generated at the expansion into the chamber and contraction out of it.

Clearly, in the approach just described one assumes that each tube is coupled independently to the expansion chamber, while in fact they are both coupled simultaneously. One also assumes that the acoustic motion remains one-dimensional and axial and, clearly, this lacks realism in many practical cases. Thus this approach is limited in application to those geometries where the experimental evidence demonstrates that the resulting model provides a sufficiently realistic first approximation. As noted later in section 4.2.1, consistently realistic models of the acoustic behaviour of flow-reversing chambers requires further extensive study and development.

2.3. THE ACOUSTIC PRESSURE DISTRIBUTION IN THE CENTRAL ELEMENT

The solutions of equation (5a), describing the acoustic pressure distribution in the central section of the silencers in Figure 3, follows a common procedure, but there are changes in some of the details that reflect their individual geometry. After having evaluated a set of six boundary conditions at points 5–9 in Figure 3, they are substituted back into equations (5) to establish a set of six simultaneous equations which can be solved for the six pressure amplitudes B_{2n}.

2.3.1. *The cross-flow chamber*

With reference to Figure 3(a), one notes that the origin for x is at the outlet position 9, so $x = 0$ at positions 7, 8, and 9, interfacing with regions 1, 2 and 3 respectively. Also $x = -l$ at positions 5 and 6, interfacing with regions 2 and 3. The Mach number is equal to M_1 at position 4, and M_3 at 9, but zero at 5–8. The amplitudes of the component pressures p_9^+ and p_9^- are known at position 9 but not elsewhere. Across the outlet plane at 9 continuity of pressure and conservation of momentum, from equation (7f), are expressed respectively as

$$\sum_{n=1}^{6} B_{2n}\phi_{3n} = p_9^+ + p_9^-, \qquad \sum_{n=1}^{6} B_{2n}\phi_{3n}\psi_{3n} = (p_9^+ - p_9^-)/\rho_9 c_9, \tag{8a,b}$$

and at positions 5–8, conservation of momentum from equation (7b) is expressed by

$$\sum_{n=1}^{6} B_{2n}(\lambda_n\zeta_5 + \mathrm{i}k)\exp(-\lambda_n l) = 0, \qquad \sum_{n=1}^{6} B_{2n}\phi_{3n}(\lambda_n\zeta_6 + \mathrm{i}k)\exp(-\lambda_n l) = 0, \tag{8c,d}$$

$$\sum_{n=1}^{6} B_{2n}\phi_{1n}(\lambda_n\zeta_7 + \mathrm{i}k) = 0, \qquad \sum_{n=1}^{6} B_{2n}(\lambda_n\zeta_8 + \mathrm{i}k) = 0. \tag{8e,f}$$

The six simultaneous linear equations (8a)–(8f) are then solved for B_{2n}, $n = 1, \ldots, 6$. The relevant vectors B_{jn} are then evaluated for regions 1 and 3 and inserted into equations (5), thus establishing the acoustic pressure distribution throughout the central element of the cross-flow chamber.

2.3.2. *The cross-flow reversing chamber*

With reference to Figure 3(b), at positions 5 and 6, $x = 0$, while at positions 7, 8 and 9, $x = l$. Also again the Mach number equals M_1 at position 4, but it is now M_3 at position 6, while the direction of flow has been reversed. At the remaining positions it is again zero. Continuity of pressure and conservation of momentum at position 6 are expressed, respectively, by

$$\sum_{n=1}^{6} B_{2n}\phi_{3n} = p_6^+ + p_6^-, \qquad \sum_{n=1}^{6} B_{2n}\phi_{3n}\psi_{3n} = (p_6^+ - p_6^-)/\rho_6 c_6. \tag{9a,b}$$

At the two ends of the central region 2 of the expansion chamber, at $x = 0$ and now at $x = l$, after applying equation (7b), conservation of momentum is expressed, respectively, by

$$\sum_{n=1}^{6} B_{2n}(\lambda_n\zeta_5 + \mathrm{i}k) = 0, \qquad \sum_{n=1}^{6} B_{2n}(\lambda_n\zeta_8 + \mathrm{i}k)\exp \lambda l = 0, \tag{9c,d}$$

and similarly at the right-hand ends of the inlet and outlet pipes, respectively, when $x = l$ by

$$\sum_{n=1}^{6} B_{2n}\phi_{1n}(\lambda_n\zeta_7 + \mathrm{i}k)\exp \lambda l = 0, \qquad \sum_{n=1}^{6} B_{2n}\phi_{3n}(\lambda_n\zeta_9 + \mathrm{i}k)\exp \lambda l = 0. \tag{9e,f}$$

Equations (9a)–(9f) are solved for B_{2n} by the same procedure. Following this, the appropriate values of B_{jn} are substituted in equations (5), to establish the pressure distribution in the central element of the cross-flow reversing silencer.

2.3.3. *The cross-flow silencer with parallel paths*

With reference to Figure 3(c), the geometrical arrangement of the central element is similar to that in Figure 3(b), but the Mach number is no longer zero but is now equal to M_1 at position 7 and M_3 at position 9. For this case, equations (9e) and (9f), after making use of equation (7b), are replaced by

$$\sum_{n=1}^{6} B_{2n}\phi_{1n}(\lambda_n(\zeta_7 + M_1) + \mathrm{i}k) \exp \lambda l = 0,$$

$$\sum_{n=1}^{6} B_{2n}\phi_{3n}(\lambda_n(\zeta_9 + M_3) + \mathrm{i}k) \exp \lambda l = 0, \tag{10e,f}$$

while the remaining four equations (10a)–(10d) describing continuity of pressure or conservation of momentum for this geometry are the same as the corresponding equations (9). After having solved equations (10) for B_{2n}, the appropriate values of B_{jn} are substituted in equations (5) to describe the acoustic pressure distribution in central perforated element of the cross-flow reversing chamber with parallel flow paths.

2.3.4. *The triflow silencer*

With reference to Figure 1(d), it is clear that equations (10) describing continuity of pressure at position 6 and conservation of momentum at this and the other four positions also apply to the central element of the triflow. One notes that proper account of the presence or otherwise of a Helmholtz resonator attached to the flow resonator should be included in the evaluation of the two relevant reflection coefficients r_7 and r_9. The remaining component of the triflow geometry, namely the flow-reversing chamber leading to the tailpipe, will have been taken into account when evaluating the two component pressures p_6^+ and p_6^- at the outlet of the central perforated element.

2.4. THE VELOCITY DISTRIBUTION IN THE CENTRAL ELEMENT

To complete the set of acoustic models of the silencers illustrated in Figure 1, one must first establish the distribution of fluctuating acoustic velocity throughout the central perforated section. To do so, one can combine the relevant form of equation (7c), describing conservation of momentum, with equations (5), leading to

$$(p_j^+ - p_j^-) = \sum_{n=1}^{6} - B_{jn}\lambda_n \exp(\lambda_n x)/(M_j\lambda_n + \mathrm{i}k_j), \qquad j = 1,\ 2,\ 3, \tag{11}$$

in the relevant region j at the axial co-ordinate positon x. Normally, to describe the overall acoustic performance of the central acoustic element, one needs only to calculate the velocity and pressure at the inlet plane, position 4. From equation (5a), for example, the pressure is given by

$$p_4 = p_4^+ + p_4^- = \sum_{n=1}^{6} \phi_{1n}B_{2n} \exp(\lambda_n x_4), \tag{12a,b}$$

while the velocity, after making use of equation (7e), is given by

$$u_4 = (p_4^+ - p_4^-)/\rho_4 c_4 = \sum_{n=1}^{6} \phi_{1n} B_{2n} \psi_{1n}. \tag{12c,d}$$

Equations (12a) and (12c) can be solved for p_4^+ and p_4^-, leading to

$$2p_4^+ = p_4 + \rho_4 c_4 u_4, \qquad 2p_4^- = p_4 - \rho_4 c_4 u_4. \tag{13a,b}$$

The acoustic velocity and pressure at any other point in the three regions of the central element of the silencers in Figures 1 and 3 can be calculated by appropriate substitutions in equations (5) and (7e). After having done this, the corresponding component wave amplitudes p^+ and p^- can be calculated for that point with equations (13a,b).

2.5. ACOUSTIC TRANSFER FROM SILENCER OUTPUT TO INPUT PLANES

To complete the predictive models for the silencers in Figure 1, one needs to include the transfers from the silencer output plane to the output plane of the central section and similarly from its input plane to the silencer input plane. Since the necessary information is available in terms of the complex amplitudes of the positively travelling p^+ and negatively travelling p^- component waves at the relevant positons, this is a straightforward procedure for the four examples in Figures 1(a)–1(c), where the corresponding transfers are along known lengths of uniform pipe. With the triflow example illustrated in Figure 1(d), one needs to calculate the transfers along the appropriate length of the uniform tailpipe and then via the flow-reversing expansion to the outlet plane at position 6 in Figure 3(b). Methods for calculating such transfers in expansion chambers can be found in reference [4].

2.5.1. *Silencer acoustic performance*

It is often convenient to summarize the acoustic performance of silencers by spectral descriptions of their acoustic transfer characteristics. If the predicted wave component amplitudes at the inlet plane are p_I^+ and p_I^- respectively, while those at the outlet plane are p_0^+ and p_0^-, then a simple performance index [4] is the attenuation index AL, defined by

$$AL = 20 \log_{10} |p_I^+|/|p_0^+|. \tag{14}$$

Another is the acoustic power loss index WL, expressed for plane waves by

$$WL = 10 \log_{10}(W_I/W_0), \tag{15a}$$

where

$$W_I = (S_I/\rho_I c_I)[(1 + M_I)^2 |p_I^+|^2 - (1 - M_I)^2 |p_I^-|^2], \tag{15b}$$

and S_I is the cross-section area, while W_0 is evaluated by the corresponding expression to equation (15b).

Acoustic performance is commonly described by the transmission loss index TL, which for an acoustic element is formally defined as the difference in sound power in free space between that incident on and that transmitted across it, and is then an invariant property of the element. When applying this definition to the flow duct situation, and taking account of the presence of both incident and reflected waves, then TL is similar to WL.

However, in many cases it is assumed that the termination at the silencer outlet is anechoic, so that

$$TL = 10 \log_{10}(W_I/W_0'), \tag{16a}$$

where

$$W_0' = S_0/\rho_0 c_0[(1 + M)^2|p_0^+|^2], \tag{16b}$$

since p_0^- is then zero. This clearly does not correspond to the normal installed performance of any silencer in a practical situation. Furthermore, since the acoustic pressure $p = p^+ + p^-$ varies cyclically with axial position along a uniform pipe, while the individual wave component magnitudes of the $|p^+|$ and $|p^-|$ remain effectively independent of position, equations (14), (15) or (16) seem likely to provide a more consistent comparison of predicted with measured performance, than measurements of the fluctuating pressure on either side of the element, unless appropriate precautions are taken while performing the measurements or the calculations.

Another alternative is to model the acoustic behaviour [7] by an appropriate transfer matrix T. A scattering matrix, for example, is a square 2×2 matrix with the four elements T_{11}, T_{12}, T_{21} and T_{22} and then

$$p_1^+ = T_{11}p_2^+ + T_{12}p_2^-, \qquad p_1^- = T_{21}p_2^+ + T_{22}p_2^-. \tag{17a,b}$$

Measurements or calculations with an anechoic termination, so that $p_2^- = 0$, suffice to establish the values of T_{11} and T_{22}, but a second measurement or calculation is then required to find the values of T_{21} and T_{12}. A popular alternative is to adopt the equivalent so-called impedance matrix, relating the transfer of acoustic pressure p_1 and velocity u_1 at inlet to the corresponding values p_2 and u_2 at outlet. The same requirements obviously apply to the evaluation of four elements of this matrix.

2.6. COMPUTATION

The realism of the predicted results will depend on a number of factors. Some of these, such as the relative precision with which the geometric detail and flow and gas properties are specified, are obvious. Others, such as the influence of viscothermal losses to the pipe walls, and the influence of entropy changes at area discontinuities [4] have been described elsewhere. Other factors, including the specification of perforated wall impedance that is described in Appendix B, with the acoustic transfers at flow-reversing chambers briefly discussed later, also have a significant influence on the realism of the predictions.

Experience has shown that rounding errors, or the occurrence of numerical overflow, or of underflow, during the numerical calculations, can also present problems. The precautions required for the successful extraction of the roots λ_n describing the wavenumbers in the central perforated element have already been described. It was found that these roots can have positive and negative parts which can be sufficiently large to cause overflow or underflow when computing the values of the factor $\exp(\lambda_n x)$ that was present in many of the equations involving B_{jn}. Thus, as with those concerned with the extraction of the roots, all these calculations should be performed with adequate precision to avoid such numerical problems. Practical experience indicates that double precision is normally adequate with the 32-bit processors installed in contemporary desktop computers.

Although the measurements described here were performed at ambient conditions, the predictive code written in Fortran and implemented in the computer [8] included appropriate provision for the existence of flow temperature and static pressure gradients normally present in any practical application. Similarly, the code included appropriate

modelling of the Helmholtz resonators shown in Figure 1(d), while the corresponding experimental validation appears in references [8, 9].

3. SILENCER ATTENUATION PERFORMANCE

The attenuation performance defined in equation (14) was both measured and calculated for a systematic sequence of silencers representing the range of silencer types illustrated in Figures 1(b)–1(d). Attenuation performance [8] was adopted to describe acoustic behaviour for reasons set out in section 2.5.1. For each type, certain geometric features are known to modify their acoustic behaviour significantly, so the relative influence of several of these factors was included in the investigation. For example, the tailpipe length is well known to modify the spectral distribution of attenuation peaks and troughs; also the ratio of chamber to pipe cross-section areas, or the expansion ratio, is a factor that often controls the general levels of the spectral peaks, while the porosity of the perforated pipes is one of the factors directing the paths followed by the gas flow and the propagation of acoustic energy, and thereby has a direct influence on acoustic behaviour. Finally, to establish the influence of mean flow on acoustic performance, measurements were made at flow Mach numbers ranging from $M = 0$ to $M = 0{\cdot}1$. The relevant geometric features of all the model silencers are set out in Appendix C.

Sets of measurements of silencer attenuation performance were completed on a sequence of some 20 model silencers. The results presented here were chosen from among these to illustrate the relative influence on silencer performance of the various factors already listed and to include others that are also often significant. The aim was to provide appropriate physical insight either to verify or improve the modelling and thereby the realism of the resulting predictions, or to guide design choice and detail when developing and refining an optimum exhaust system design relevant for each practical application. Thus one primary aim of the measurements was to establish a database identifying the relationships between observed acoustic behaviour and the layout, with the detailed arrangements of the silencer element's geometry. Another was to use the observations to validate the predictive models described in section 2, and assess their realism for application to practical design development and assessment.

3.1. CROSS-FLOW SILENCER ELEMENTS

Two silencers of the type shown in Figure 1(b) were selected, with both the expansion ratio and the porosity of the first double that of the second. Comparisons of their measured and predicted performance then gave some information on the relative influence of these two factors on silencer acoustic performance. The attenuation performance of the first labelled silencer, no. 1, is presented in Figure 4 and of the second labelled silencer, no. 2, in Figure 5.

Comparisons between measurements and predictions for cross-flow silencer no. 1 with zero flow are represented in Figure 4(a). The data was recorded with the shorter data lengths and at the lower sampling rate of the two sets defined in Appendix A. The hairy appearance of the results at the higher attenuation peaks is probably an artefact of the resulting limit in the number of spectral averages that was possible with this length of data record, so the higher sampling rate with the longer data record was used for the remainder of the measurements. This appearance was also traced to the limited dynamic range that resulted from the relatively low output of the source between 500 and 600 Hz and above 800 Hz. The attenuation minima at 163, 325, 490, 655, 820 and 980 Hz all correspond to the half-wave resonances of the tailpipe with acoustic length of 1·01 m plus the end correction [4] to be added at the open termination. This varied between 14 and 12 mm over

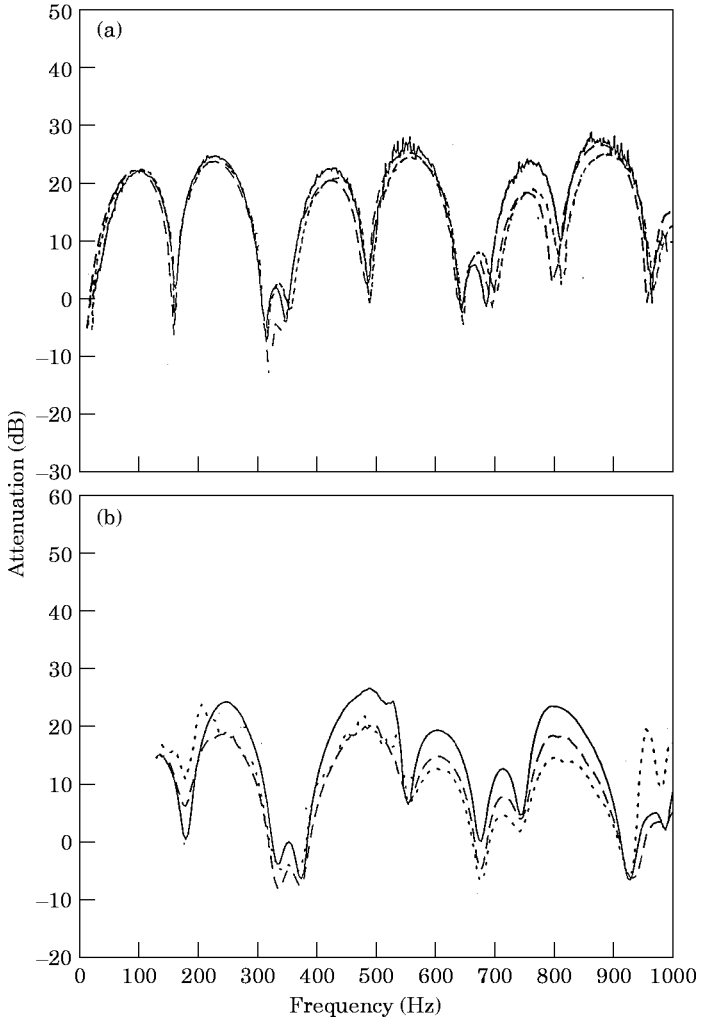

Figure 4. The attenuation of cross-flow silencer no. 1; perforate 15·9% porosity. (a) Zero flow, tailpipe 1·01 m: ———, measured; — — —, predicted; ----, predicted without perforate present. (b) With flow, tailpipe 0·874 m, ———, M = 0; — — —, M = 0·05; ---, M = 0·1.

the frequency range shown giving a total acoustic length of 1·024–1·022 m. (But see also the discussion in section 4.2.) The area expansion ratio between pipe and chamber was 15·6, while one can see that the peak observed attenuation in Figure 4(a) was close to 20 log 15·6 or 24 dB. This also corresponds to the value one would anticipate [7] with an open chamber after the perforated pipes had been removed! Predictions both with the model described in section 2.3.1 and with an open chamber [4], that is, with perforate pipes omitted, are also both included in Figure 4(a). The close agreement between the two predictions and also with the measurements suggests that pipes with a wall porosity of 15·9 percent have a sufficiently open surface to be effectively acoustically transparent. Thus all but one of the other model silencers were constructed with perforated pipes with the significantly lower porosity of 6·8 percent.

The attenuation performance of the same silencer both with flow and with a shorter tailpipe is presented in Figure 4(b). The source of white noise excitation was also changed to a much more powerful driver which, however, now had a limited output below 150 Hz

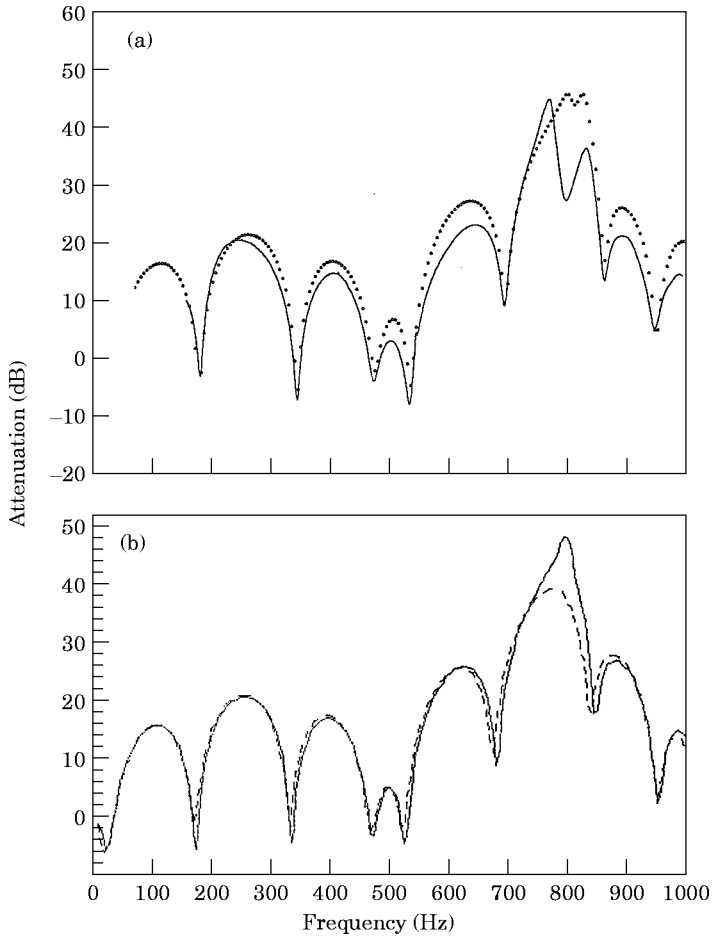

Figure 5. The attenuation of cross-flow silencer no. 2; perforate 6·8% porosity. (a) Zero flow, tailpipe 1·017 m: ———, measured; • • • • •, predicted. (b) Predicted: ———, zero flow; — — —, Mach number = 0·1.

and above 950 Hz. The significantly higher levels of excitation that resulted were required to reduce the relative contamination by flow noise sources. One notes that the shorter tailpipe raised the frequency of attenuation minima by some 15 percent. The influence of flow is clearly to reduce the measured overall acoustic performance, by up to 10 dB at $M = 0{\cdot}1$. This seems to be in contrast with published predicted transmission loss performance spectra in the literature, which tend to indicate a significant increase with flow. Further discussion of this seemingly paradoxial behaviour has been postponed until sections 3.4 and 4.1.2.

In Figure 5(a) is presented the zero flow attenuation performance of cross-flow silencer no. 2, where the perforate porosity was reduced from 15·9% of silencer no. 1 to 6·8% and the area expansion ratio was similarly reduced from 15·6 to 8·55. This provides a lower predicted open chamber peak attenuation of 18·5 dB. The tailpipe length was 1·017 m, while the open end corrections were some 2 mm less, so tailpipe resonance frequencies were slightly reduced in comparison with those in Figure 4(a). However, one can clearly see that the shape of the attenuation spectrum is now significantly different between 700 and 900 Hz, indicating the strong influence over this frequency band of the perforated walls

on both the measured and predicted performance. Although the performance was not measured with flow, the two curves plotted in Figure 5(b) show the predicted change in attenuation performance produced by a flow at a Mach number of 0·1. Comparison with Figure 4(b) shows that the reduction in peak attenuation by 10 dB matches the result there, but at the minima at 170 and 340 Hz the results do not quite correspond. Thus there is an increase in attenuation of 5 dB for both in Figure 5(b), in contrast to an increase of 10 dB at the corresponding lower frequency minima, but a reduction of 10 dB at the higher frequency minima in Figure 4(b)!

One should note that the zero flow predictions in Figure 5(a) differ in detail at 800 Hz from the corresponding ones in Figure 5(b). The relevant calculations were performed respectively on an IBM type 486 and a Macintosh type SE/30, where the corresponding processors and thus their associated rounding errors were not the same.

3.2. FLOW-REVERSING SILENCER ELEMENTS

The measurements with the flow-reversing silencers are presented in two main groups. With the first group, the dimensions of the central section geometry remained effectively the same as those for cross-flow silencer no. 2. The first silencer in this group, no. 2(R), is in fact no. 2 with the tailpipe transferred from the outlet to the inlet end, so it represents the geometric arrangement in Figure 1(bR). Silencer no. 2(c) has a flow-reversing chamber added along the lines shown in Figure 1(c), while no. 2(d) has been converted to a triflow by appropriate additions of a second flow-reversing chamber and longer tailpipe passing through the expansion. This group of measurements with the associated predictions thus provides comparative information on the characteristic acoustic behaviour of the three types of silencer layout.

The measurements and predictions, all for zero flow, are assembled together in Figure 6. The measured attentuation performance of silencer no. 2(R) with zero flow is presented in Figure 6(a), with the corresponding prediction for comparison. Since the tailpipe length is the same as with silencer no. 2, the frequencies of the associated attenuation minima are the same as those in Figure 5(a). Otherwise, comparison of the two measurements reveals several differences. There is a general rise averaging at least 5 dB in attenuation right across the spectrum. Between 200 and 500 Hz which includes the high peak at 365 Hz it exceeds 10 dB: on the other hand, over a band centred at 800 Hz there is a reduction in attentuation of about the same magnitude. One is tempted to draw a parallel between the contrasting acoustic behaviour of these two silencers with the resonant behaviour of acoustic elements of the same length, that are either open at both ends or have one end closed.

Comparison of the measurements in Figure 6(b) with those in Figure 6(a) shows that the addition of the flow-reversing chamber, to convert silencer 2(R) to 2(c), has produced little further change in acoustic performance. The systematic increase in the frequency of the minima is most probably due to the reduction of the tailpipe length from 1·0174 m to 0·973 m. In both of these two examples a fair to good correlation exists between the predictions and the observations. The differences in level between observation and prediction at the high attenuation peaks could well be ascribed to small differences between the actual and assumed wave damping and other losses during the calculations. This is supported by the good agreement shown at lower levels of attenuation. Alternatively, it could be due to the relative reduction in the reflection coefficient at the closed end of the central element in silencer 2(c).

Comparison of Figure 6(c) with Figure 6(b) demonstrates the changes in acoustic performance that accompany the addition to a further flow-reversal element with almost half a metre to the length of the tailpipe. These additional components have raised the

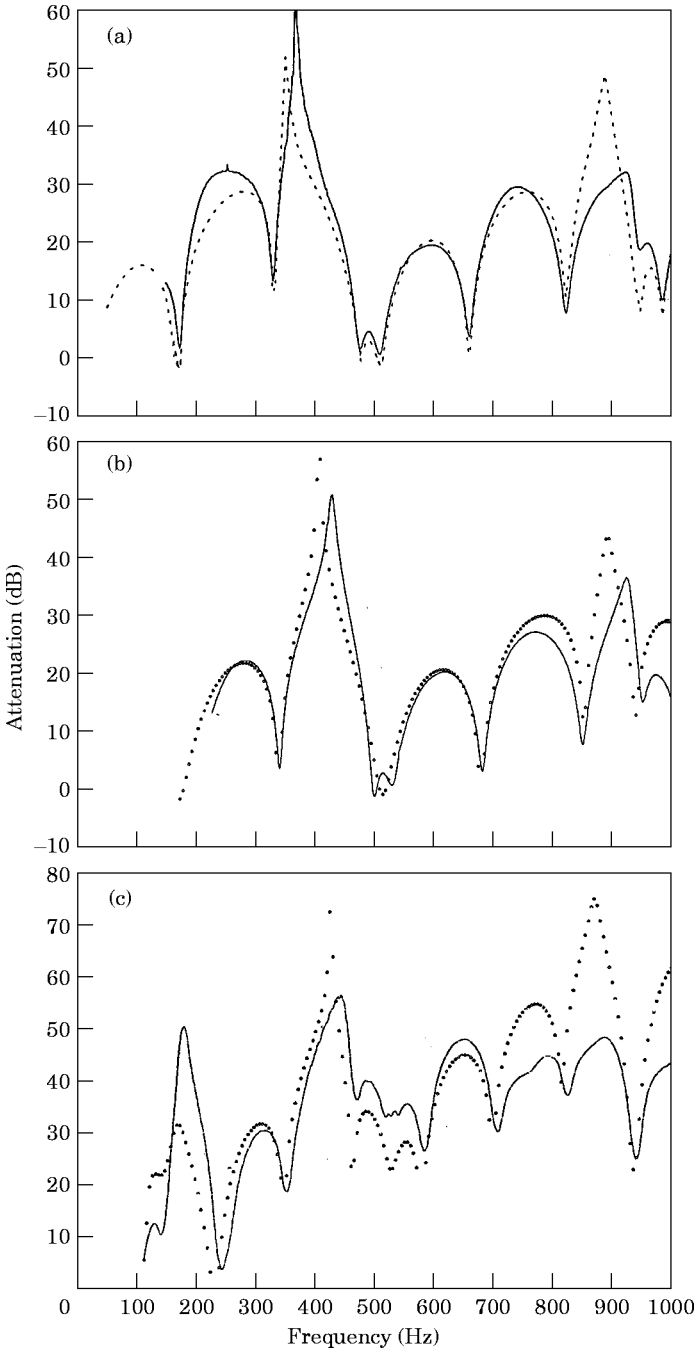

Figure 6. The comparable attenuation of flow-reversing silencers, with "identical" central sections. (a) Cross-flow reversing 2(R), tailpipe 1·017 m: ———, measured; — — —, predicted, (b) Cross-flow with parallel paths 2(c), tailpipe 0·973 m: ———, measured; • • • • •, predicted. (c) Triflow 2(d), tailpipe 1·43 m: ———, measured; • • • • •, predicted;

general level of attenuation by some 15 dB above 300 Hz; for example, the minimum attenuation of 5 dB near 350 Hz in Figure 6(b) has risen to 20 dB in Figure 6(c), while a new peak of 50 dB has appeared at 200 Hz. However, this is accompanied by a new minimum of 250 Hz at 5 dB in Figure 2(c), compared with a level of some 20 dB in Figure 2(b). Although, as should be expected, the predicted frequencies and corresponding levels of the attenuation minima for the triflow in Figure 2(c) are similar to the measured ones, the predicted levels of the higher peaks do not match so well, there being overprediction at some with the reverse at others. Nevertheless, the acoustic performance at the minima is of much greater practical significance in terms of the overall installed exhaust system attenuation achieved under vehicle operating conditions, so the agreement at the spectral minima is of more practical relevance.

3.3. SIDE BRANCHES

The spectral distribution of the attenuation with the overall performance of all expansion chamber silencers is strongly influenced [8] by the addition of annular side branches within the expansion. The fact that one must provide sufficient lengths of perforated pipe to accommodate the flow without incurring excessive back pressure means that the scope for adding this feature to cross-flow silencers is somewhat limited. The fact that side branches can certainly modify the acoustic behaviour is illustrated by comparing Figure 7(a) with Figure 6(a) and Figure 7(b) with Figure 6(b).

For the results in Figure 7, the inlet side branch length was reduced from 0·084 m to 0·026 m, while that at the other end was increased from 0·024 to 0·134 m, to convert silencers no. 2(R) and no. 2(c) to silencers no. 2(R1) and no. 2(c1) respectively, as has been listed in Appendix C. The tailpipes here are also 0·1 m shorter, although the change was not made deliberately. The resulting shift of the associated frequencies of the successive spectral minima, by an amount inversely proportional to the respective reduction in tailpipe length, again shows that these features of the attenuation spectra are related to the tailpipe. On the other hand, the frequency of the major peaks has been reduced, for example, from 365 Hz in Figure 6(a) for silencer 2(R) to 290 Hz in Figure 7(a) for silencer no. 2(R1), with a rather larger reduction for silencer 2(c1) compared with silencer 2(c) in Figures 7(b) and 6(b) respectively.

However, the overall acoustic performance of both silencers has remained effectively the same following the change in side branch lengths. The predictions on Figure 7(a) are a fair match with the observations, except for the magnitude of the predicted attenuation at the tailpipe minima, which is obviously misleading. The match of Figure 7(b) is similarly acceptable below 700 Hz at the peaks but again not so at the minima. The minima correspond to the acoustic resonances of the system, and the predicted levels there are thus rather sensitive to the effective damping at these frequencies. It seems likely that the 20% reduction in the length of perforated pipes reduced this significantly for the preditions, but not for the measurements. These two results are representative of several other similar comparisons, and indicate the relative sensitivity of the frequency and amplitude distribution of the attenuation spectrum to changes in the internal geometry of the central chamber.

3.4. MEASURED ATTENUATION SPECTRA WITH FLOW

Sequences of attenuation spectra measurements at $M = 0$, $M = 0{\cdot}05$ and $M = 0{\cdot}1$ were made with at least ten different silencers and revealed rather similar trends in the general behaviour of all of them. One typical example with cross-flow silencer no. 1 has already been given in Figure 4(b) and two more are now presented in Figures 8(a) and 8(b), again corresponding to silencers 2(R1) and 2(c1) respectively. Here, the zero flow measurements

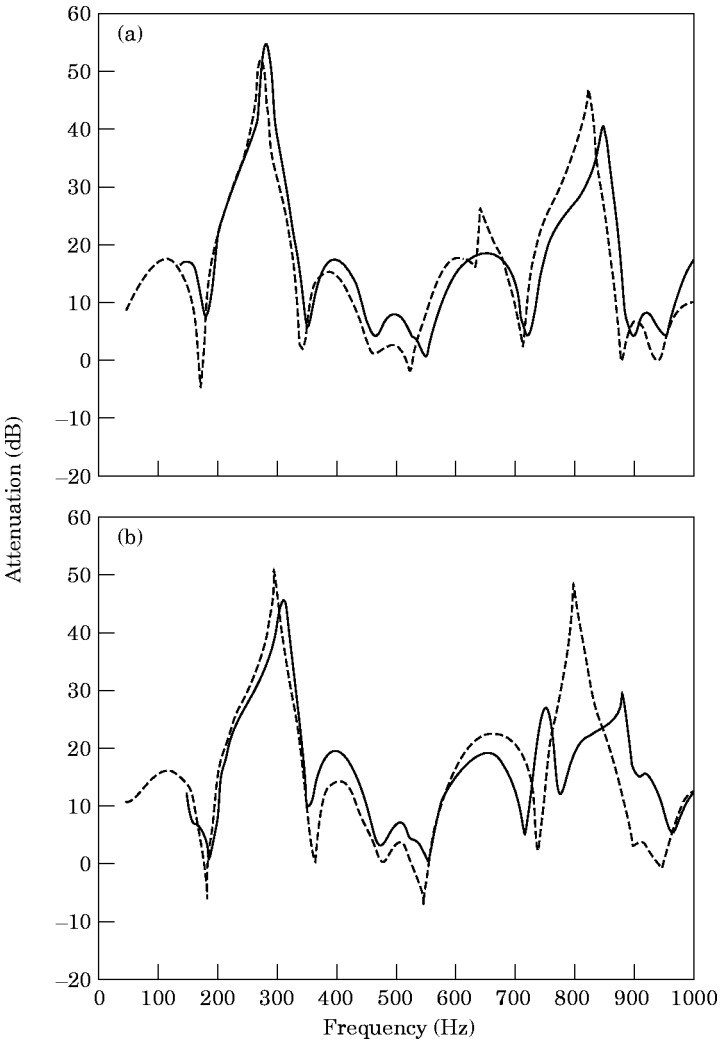

Figure 7. The comparative attenuation of flow-reversing silencers with altered internal side branches. (a) Cross-flow reversing 2(R), tailpipe 0·915 m: ———, measured; — — —, predicted. (b) Cross-flow with parallel paths 2(c1), tailpipe 0·915 m: ———, measured; — — —, predicted;

in Figures 7(a) and 7(b) are repeated for comparison with measurements made with flow Mach number $M = 0{\cdot}05$ and $M = 0.1$. Except at the high attenuation peaks found with zero flow, there is a general trend for attenuation levels to increase with flow velocity, although there are some exceptions to this, in particular above 900 Hz. Similar trends in behaviour were found in nearly all cases, except perhaps for the results in Figure 4(b) at the attenuation minima. It can be argued that the reduction in attenuation at the high peak levels might be due to flow noise generation, since the pressure signal amplitude in the tailpipe is inversely proportional to the attenuation, while it is generally well established that, other things being equal, flow noise levels tend to be higher in the tailpipe than elsewhere in the system.

It seems well established by all the measurements, including those not illustrated here, that the major influence of flow, excluding the generation of sound by the associated aeroacoustic sources [9], is to flatten out the attenuation spectra to some extent, at least

over the Mach number range investigated here. It is common experience that flow noise generation normally leads to some deterioration of overall attenuation performance of exhaust systems that increases with flow Mach number. The consistent deterioration in the attenuation performance above 900 Hz in all the current observations suggests that flow generated noise was responsible for this feature.

3.4.1. *The influence of throughflow on perforate impedance*

The influence of perforate impedance on the reactive acoustic behaviour is rather complex, though both predictions and observations indicate that a general reduction of attenuation levels at spectral peaks with a corresponding rise in level at spectral minima accompanies an increase of perforate impedance. No such trends are evident in the observations presented in Figures 7(b) and 8(b) despite the addition of an additional flow path reducing the flow velocity through the perforate for the results in Figure 8(b) compared with those in Figure 7(b). Further increase of flow velocity through the perforate

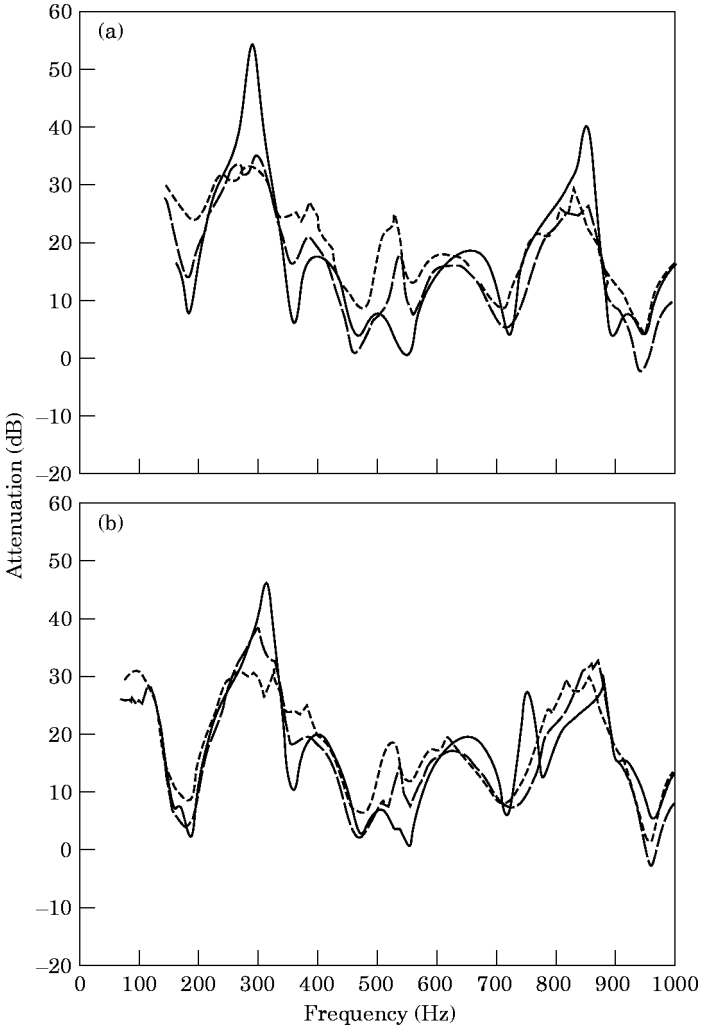

Figure 8. The influence of flow on attenuation performance. (a) Silencer 2(R1): ———, M = 0; — — —, M = 0·05; ----, M = 0·1. (b) Silencer 2(c1): ———, M = 0; — — —, M = 0·05; ----, M = 0·1.

by some 25 percent by reducing the area of the perforate in the cross-flow silencer 2(R1) led to a similar result. This evidence also supports the assumption adopted in Appendix B that perforate impedance is not significantly altered by varying the mean flow through it, at least for the range of variation that existed in the percent series of experiments where the throughflow Mach numbers in the holes were as high as 0·09 in some instances. This result seems consistent with both the predictions and measurements reported in reference [1] for a silencer of type illustrated in Figure 1(a) after due allowance was taken for the different method adopted for calculating the hole impedance (but see also the discussion in section 4.1.2). In this case the porosity was 3·9% and the average flow Mach number through the holes was 0·12.

3.4.2. *Flow-reversing end chambers*

When present, such chambers will clearly have an influence on silencer acoustic behaviour. Thus the attenuation spectra of flow-reversing chambers were investigated in a separate sequence of experiments with four different geometrical arrangements in each of two chambers of different sizes. As with the cross-flow silencers, they all exhibited similar acoustic behaviour at the attenuation minima as the mean flow Mach number was increased from 0 to 0·1. A typical set of measurements with the larger sample is plotted in Figure 9. Below 500 Hz, the measurements show an increase in attenuation at the spectral minima with flow, while at higher frequencies the trend is reversed. The additional two minima that were clearly present at $M = 0{\cdot}1$ are a feature confined to the larger model chamber, since it did not occur with the smaller one. In seven cases there was a systematic decrease in the levels at the attenuation maxima both with increase of flow and frequency, as seen in Figure 9. However, in one set of experiments with the smaller model the trend was reversed at the highest flow speed, with no significant changes in the levels at the attenuation maxima with the flow speed at $M = 0{\cdot}05$.

3.5. RELATIVE ACOUSTIC EFFICIENCY

Since space for the sound attenuating elements of an exhaust silencing system is often severely limited, the relative acoustic efficiency of the different types in Figure 1, expressed

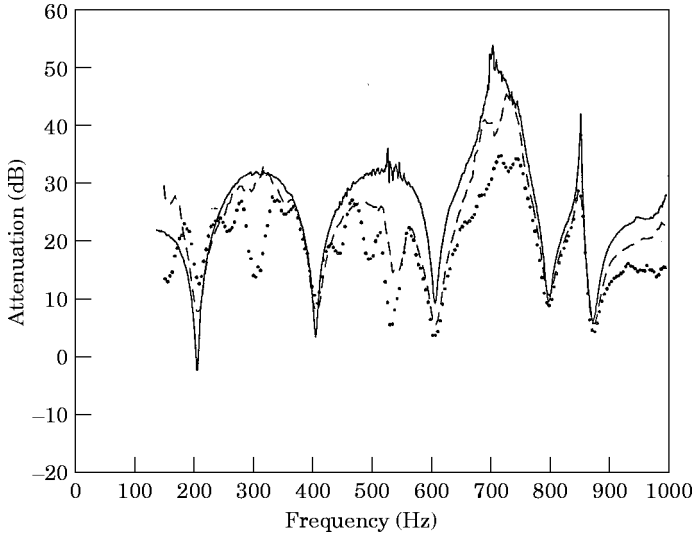

Figure 9. The attenuation performance of a flow-reversing end chamber; M = 0; tailpipe 0·8 m long: ———, – – –, M = 0·05; • • • • •, M = 0.1.

as the attenuation performance per unit volume [8], is of general interest. As has been seen the attenuation minima are normally closely associated with the half-wave resonances of the tailpipe, interacting acoustically with the preceding silencing element, so its length often governs the spectral distribution of minima in their combined attenuation performance. The measured attenuation of triflow silencer no. 1(a), with the same external dimensions as silencer no. 1, is compared with the predicted attenuation in Figure 10(a). One notes that the predictions slightly underestimate the attenuation at the minima as usual. Otherwise, the spectral distribution and levels of the remainder of their attenuation spectra match quite well, excepting the obvious local discrepancies near 350 and 800 Hz. The corresponding spectra measured with flow Mach number $M = 0$ and $M = 0.05$ are compared in Figure 10(b). One notes that the tailpipe length had been increased by 5 mm for these measurements. It is clear that the influence of flow on attenuation performance corresponds with the results described already.

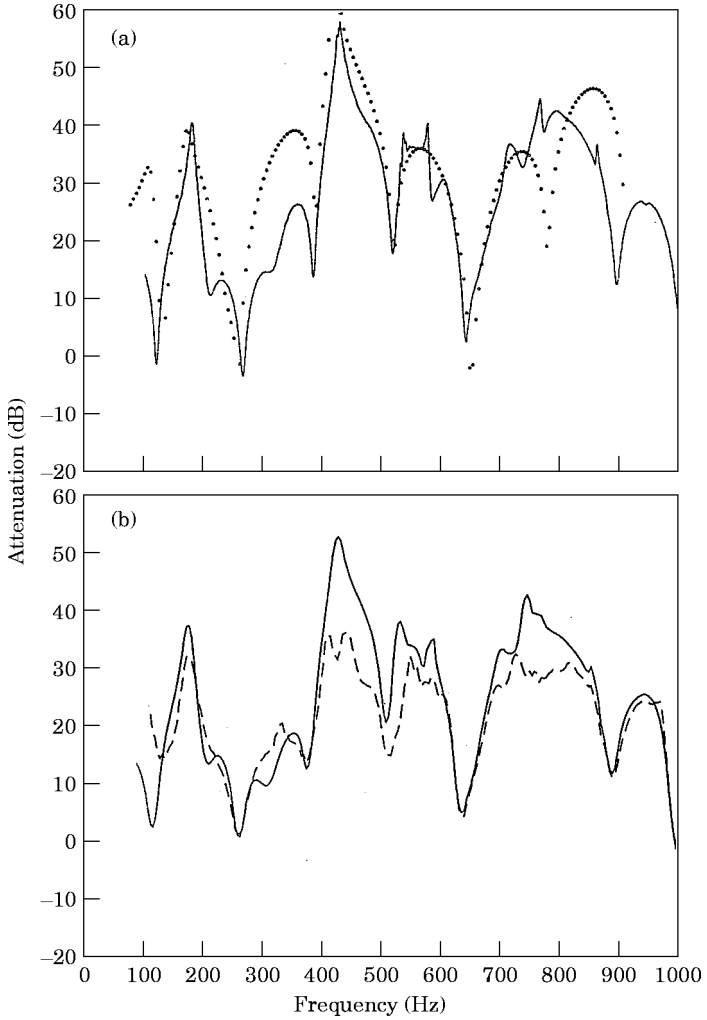

Figure 10. The attenuation performance of a triflow silencer no. 1(a). (a) With zero flow, tailpipe 1·295 m long: ———, measured; • • • • •, predicted. (b) Tailpipe 1·30 m long: ———, M = 0; – – – M = 0·05.

The relative acoustic efficiency of the triflow silencer compared with the cross-flow is demonstrated by comparing the observations in Figure 10 with those in Figure 4. When doing so one should recall that the triflow tailpipe is about 50% longer than that for cross-flow, with a consequent reduction by two thirds of the frequencies of the associated attenuation minima. There is a clear gain in attenuation performance of from 5 to 15 dB at the minima, accompanied by at least a similar gain throughout the spectrum, if one excludes the obvious minimum at 1000 Hz in the triflow attenuation spectrum. Therefore, a rough index representing the overall gain in acoustic volumetric efficiency would be some 10 dB. This explains the popularity of the triflow type, despite its potentially enhanced back pressure.

4. DISCUSSION

The primary aim of this investigation was to identify and quantify the relative influence of the geometrical features of cross-flow elements on their acoustic behaviour, together with that of all additional relevant physical and operational factors, so that they can be appropriately implemented in predictive models of the acoustic performance of multiple path silencers. Such models are an essential constituent [8] of any rational procedure for the design and acoustic performance optimization of exhaust silencing systems for the control of noise emission from reciprocating engines installed in road vehicles and other plant. One notes that the overall levels of such emissions [8] are often contolled by the spectral minima in the overall system acoustic attenuation spectrum. Thus realistic predictions by the models of the frequency and level of such attenuation minima are of particular practical interest because of their relative importance. The associated flow losses [8] represent another factor of practical interest, in the assessment of exhaust system performance, due to their direct influence on engine output and fuel efficiency. However, corresponding mean pressure loss measurements were not included in this investigation, as they were not of direct relevance to the acoustic modelling.

In any exhaust or similar flow duct system, the forward and backward travelling component wave amplitudes at any frequency remain effectively invariant along the lengths of uniform pipes connecting silencer elements or other discontinuities. This is in contrast to the corresponding fluctuating acoustic pressure and velocity distribution, since their amplitudes vary cyclically along the length of such pipes as a result of wave interference. Thus the measurements and prediction procedures adopted in this investigation took full account of these two facts, and so were primarily concerned with establishing the component wave amplitudes in the uniform pipes either side of the element under consideration. Consistently with this approach, the results of both measurements with the corresponding predictions have been presented as attenuation index spectra describing the ratio of the incident to transmitted forward travelling component wave amplitudes across each element, as defined by equation (14). The amplitude of these component waves in the tailpipe leading to the open exhaust termination are of particular relevance [4] in predicting noise emission by the exhaust system to the surrounding environment.

4.1 ACOUSTIC BEHAVIOUR OF CROSS-FLOW ELEMENTS

The cross-flow central element corresponds in behaviour to that of coupled resonant systems with internal damping in which both the coupling and the internal damping are provided by the perforated walls. The observed behaviour includes the influence of the tailpipe, to which the element is strongly coupled.

4.1.1. *The influence of geometry and wall porosity*

Where the wall porosity is high, the internal coupling is relatively strong and associated damping relatively weak. Thus with cross-flow silencer no. 1 the overall behaviour of the cross-flow element with tailpipe that was illustrated in Figure 4(a) corresponds to that of a single resonant system with half-wave resonances at 343 and 686 Hz strongly coupled to the tailpipe with half-wave resonances at 166, 332, 498, 663 and 995 Hz.

When the wall porosity is halved, as in silencer no. 2, the corresponding observations in Figure 5(a) indicate that the overall behaviour now corresponds to two coupled resonant systems with resonances at 475 and 950 Hz and a strong anti-resonance at 800 Hz. Again these are strongly coupled to a tailpipe which has half-wave resonances at 173, 345, 518, 690 and 827 Hz. The corresponding behaviour when this is modified to become a flow-reversing element is illustrated in Figure 6(a). Although the spectral distribution of attenuation is similiar in some respects, the frequency of the first strong anti-resonance has been approximately halved to 367 Hz, with a second one appearing at just below 900 Hz. The interaction of the lower anti-resonance with the tailpipe has reduced the corresponding resonance frequency slightly from 345 Hz seen in Figure 5(a). The result of adding a further coupled element as shown in Figure 6(b) is to raise the anti-resonance frequencies to 430 and 930 Hz respectively. The addition of a further flow-reversing element and a longer tailpipe has added further resonances and anti-resonances, associated with the increased number of interacting resonant elements in the overall behaviour now shown in Figure 6(c).

The coupling was reduced further by decreasing the length of the perforated pipes in silencer no. 2(R) by 20%, to produce silencer no. 2(R1). The overall length of the chamber remained the same, so one of the existing internal side branches was increased in length by a corresponding amount. This reduced the first side branch resonance frequency from just over 1000 Hz to 640 Hz. The resulting measured behaviour in Figure 7(a), when compared with that in Figure 6(a), shows that the interactions with this additional resonant system has produced a further significant reduction in the frequency of the first anti-resonance of the whole system and a slight reduction in frequency accompanied by an increase in amplitude at the second. The corresponding alterations to silencer no. 2(c) to produce no. 2(c1) have resulted in a similar behaviour at the lower anti-resonance when the corresponding observations in Figure 7(b) are compared with those in Figure 6(b), but one can see that the higher one has become more complex.

The observations all without mean flow show clearly that the observed overall changes in acoustic behaviour illustrated in Figure 4(a), 5(a) and (6a)–6(c), with Figures 7(a) and 7(b), are a result of changing both the tuning of the individual coupled resonant elements and the coupling between them. Furthermore, these changes in geometry significantly modify the resulting acoustic interactions between the individual elements.

4.1.2. *The influence of flow*

The presence of flow above $M = 0{\cdot}025$ is known to increase the resistive component of the perforate impedance significantly, thus increasing the internal damping associated with the coupling between the resonant elements in the central cross-flow section. Almost all of the observations of the overall behaviour in Figures 4(b), (8a) and 8(b), and (10b) exhibit changes in the acoustic response, both at the resonances and anti-resonances, that result from the increase in the damping that accompanies an increase in the mean flow Mach number in the inlet pipe from zero to 0·1. The same is true for the general trends in the behaviour at the anti-resonances in Figure 9 for the observations made with the flow-reversing chamber. There is some evidence of flow noise generation [9] above 900 Hz

in some of the recorded spectra. Similarly, there appears to be some decrease in the damping at the resonances found in Figures 4(b) and 9, and perhaps Figure 10(b).

The results in Figure 9 on page 785 of reference [1], giving the observed and predicted transmission loss of a plug muffler, indicate a corresponding significant increase in damping at the resonances, accompanied by a large increase in attenuation at the anti-resonances when the flow Mach number was increased from zero to 0·05. The wall porosity was considerably lower, being 3·9% in this case. The chamber diameter was 101·6 mm, pipe diameter 49·3 mm with perforated pipes 128·6 mm long. The hole diameter was similar to that in the present experiments, but the wall had only half the thickness. The effective expansion ratio from pipe to chamber was just over 3, compared with 8·5 and 15·6 in the present experiments. Clearly, the significant difference in observed behaviour at the anti-resonance requires explanation and thus provides grounds for further investigation. This is reinforced by the fact that trial calculations with the current model predicted a behaviour that was closely similar to the observations in reference [1] with zero flow, but predicted that a somewhat higher damping existed at the strongest anti-resonances.

A suggestion that the results at the higher anti-resonances presented here were all contaminated with the flow noise provides an alternative explanation for the observed behaviour. However, this is not borne out by the predicted behaviour in Figure 5(b), nor is it by an extensive sequence of other measurements reported in references [4] and [8], nor in a series of further relevant predictions and observations made during the current and other investigations that have not been specifically included among the examples illustrated.

4.2. THE PREDICTIVE MODELS

The development of the predictive models corresponding to each member of the sequence of cross-flow and multiple path silencers of current interest began from the one-dimensional wave equations (2) that describe the acoustically related fluid motion associated with each section of the central element illustrated in Figure 2. These equations were derived from the more general wave equations (1) by assuming that the wave motion in each of the three regions remained essentially one-dimensional and was directed along the pipe and chamber axes, while radial propagation existed only through the perforated pipe walls. Thus it was assumed that the influence of any further radial or transverse motion remained sufficiently small to be neglected. This includes, for example, the neglect of the time delay [4] associated with the radial area expansion from the pipe surface region 1 to the chamber and the corresponding time delay associated with the area contraction from the chamber to the pipe surface of region 3.

However, systematic discrepancies existed between the values of the predicted tailpipe resonance frequencies when such time delays were omitted from the models and those values observed during the experiments. The magnitude of each discrepancy was then seen to be proportional to the corresponding frequency of the associated spectral components of the attenuation spectra. The addition of an end correction at the tailpipe inlet with length equal to the smallest distance between the two pipe surfaces effectively eliminated any difference between the observed and the predicted tailpipe resonant frequencies. Thus this end correction has been included in the models that provided the predictions that accompany the measurements in Figures 4(a), 5(a), 6(a)–6(c), 7(a) and 7(b) and 10(a). One notes that a similar end correction was found necessary [4] to account for the time delays or, alternatively, the corresponding phase lags, that were associated with the presence of the evanescent waves at area and similar discontinuities that are required to match the corresponding boundary conditions.

In all the cases illustrated here, including the further sequence of observations and predictions that were not included, there was fair to good agreement between predictions and observations at almost all the system resonance frequencies. In a few instances, for example, those described in Figures 6(a), 7(a) and 7(b), the overall attenuation at the tailpipe resonances was underpredicted, suggesting that the corresponding predicted damping was deficient by a small but significant amount.

It is well established that prediction of the resonant behaviour of coupled resonant systems at the anti-resonances is subject to far greater uncertainties than similar predictions for the resonances. This is clearly the case with the comparisons made at the large coupled anti-resonances in the present investigation. For example, there are clearly significant differences between observed and predicted behaviour at the anti-resonances in Figures 6(c), 7(b) and 10(a). Nevertheless, the models described in section 2 appear to provide reasonably reliable predictions of observed behaviour for practical application, particularly at the resonances. It is here that reliable predictions have the greatest significance for automotive silencer design.

4.2.1. *Predictive models of flow-reversing chambers*

The assumption of one-dimensional wave motion in the flow-reversing chambers also led to inconsistencies between predicted and observed acoustic behaviour in some instances. As one might anticipate, such anomalies were more likely when the aspect ratio, defined as the ratio of the chamber length to its transverse dimension, was substantially less than unity. The end correction described in section 2.2.1 eliminated the inconsistencies as long as the pipes were flush with the end bulkhead of the chamber, or were only slightly protruding from it, as is often found with manufactured silencers of the relevant type.

The extension of one of these pipes to, say, half the chamber length, thus forming an inlet or outlet side branch, introduced marked changes in the observed behaviour, with corresponding inconsistencies in the predictions, although there was often reasonable qualitative agreement. Clearly, this is an area for further investigation so as to improve the modelling and maintain realism in the predicted acoustic behaviour. Predictions with such models should also agree with any other observations [10] that already exist in the literature. However, in this case the corresponding geometry was not described in sufficient detail to perform any comparisons.

Similar inconsistencies have not been observed with the existing validated models [8] describing the acoustic behaviour of Helmholtz resonators. This includes the design of such resonators attached to expansion chambers [8] to enhance their attenuation performance to a required level at a specified frequency.

5. CONCLUSIONS

Any rational intake/exhaust system design methodology [8] depends on a clear quantitative understanding of the acoustic behaviour of the individual elements. The material presented here explores the predictive acoustic modelling of three-duct silencer configurations by one-dimensional equations. Comparisons are presented between the predicted and observed behaviour of eight representative examples chosen from the sequence of 20 model silencers tested, with geometry corresponding to the last four layouts in Figure 1. Close agreement existed between predictions and observations with the cross-flow silencers, type (b), and good agreement with the cross-flow reversing examples, type (bR). The agreement was generally acceptable for practical purposes to fairly good

with the cross-flow reverse with parallel paths type (c), but significantly less so being barely acceptable for the triflow, type (d).

The reason for this was traced to the inadequacies of one-dimensional modelling adequately to represent the acoustic behaviour of the flow-reversing expansions, since in general terms this must clearly be strongly influenced by the cross-modes that must exist there. The obvious advantages or design purpose of analytical models which maintain physical insight and take due account of flow and temperature gradients over finite element models provides the incentive for further studies in the appropriate modelling of these elements. Some progress has already been made in this direction by adopting a more physically realistic approach to the modelling.

A better detailed understanding of the lumped or distributed acoustic characteristics of the perforated tubes, both linear and non-linear, would also improve the realism of the modelling. This and the quantitative characterization of flow noise sources [9] also represents an active area of current research. Of practical significance is the established fact that, in practical terms [14], once the porosity exceeds around 15%, porous pipes are effectively acoustically transparent.

With the exception of flow noise generation, the influence of both flow and temperature gradients on acoustic performance [8, 13] appears to be adequately represented by the one-dimensional modelling, at least for practical design purposes.

REFERENCES

1. J. W. Sullivan 1979 *Journal of the Acoustical Society of America* **66**, 772–778. A method for modelling perforated tube muffler components, I and II.
2. K. S. Peat 1988 *Journal of Sound and Vibration* **123,** 199–212. A numerical decoupling analysis of perforated pipe silencer elements.
3. E. Dokumaci 1996 *Journal of Sound and Vibration* **191**, 505–518. Matrizant approach to acoustic analysis of perforated multiple tube mufflers carrying mean flow.
4. P. O. A. L. Davies 1988 *Journal of Sound and Vibration* **124,** 91–115. Practical flow duct acoustics.
5. J. L. Bento-Coelho 1983 *Ph.D. Thesis*, *University of Southampton*. Acoustic characteristics of perforate liners in expansion chambers.
6. H. Collins 1994 *M.Sc. Thesis*, *University of Southampton*. Predictive models of advanced muffler acoustic performance.
7. P. O. A. L. Davies 1991 *Journal of Sound and Vibration* **151,** 333–338. Transition matrix representation of exhaust system acoustic characteristics.
8. P. O. A. L. Davies 1996 *Journal of Sound and Vibration* **190,** 677–712. Piston engine intake and exhaust system design.
9. P. O. A. L. Davies 1996 *Journal of Sound and Vibration* **190,** 345–362. Aeroacoustics and time varying systems.
10. C. J. Young and M. J. Crocker 1976 *Journal of the Acoustical Society of America* **60**, 1111–1118. Acoustical analysis, testing and design of flow reversing muffler chambers.
11. A. F. Seybert and D. F. Ross 1977 *Journal of the Acoustical Society of America* **61**, 1362–1370. Experimental determination of acoustic properties using a two-microphone random excitation technique.
12. P. O. A. L. Davies, M. Bhattacharaya and J. L. Bento Coelho 1980 *Journal of Sound and Vibration* **72,** 539–542. Measurement of plane wave acoustic fields in flow ducts.
13. M. F. Harrison 1994 *Ph.D. Thesis*, *University of Southampton*. Time and frequency domain modelling of vehicle intake and exhaust systems.
14. F. Kunz 1974 Private communication.

APPENDIX A: FOUR-MICROPHONE WAVE DECOMPOSITION

The acoustic performance of silencers was summarized in section 2.5 by spectral descriptions of their predicted acoustic transfer characteristics. These were expressed in

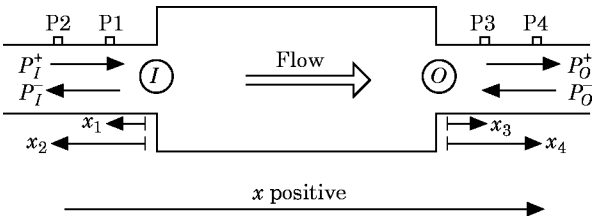

Figure 1A. The four-microphone test layout.

terms of the positively and negatively travelling component wave spectra $p^{\pm}(\omega)$. Corresponding measurements are required for comparison with predictions. Although experimental procedures for performing such measurements are well documented [11, 12] there are some differences [12] in detail in those adopted for the measurements reported here. The positions of the inlet I and outlet O planes of the element of interest are first identified as shown in Figure A1. Two pairs of pressure time histories, P_1 and P_2 in the inlet duct leading to plane I and P_3 and P_4 in the outlet duct following from plane O, are measured simultaneously at positions x_1, x_2 and x_3, x_4 respectively relative to planes I and O, as shown in the figure. It should be noted that x_1 and x_2 have negative values, while those for x_3 and x_4 are positive.

The acoustic fields at the four transducers are the complex sum of the individual positively and negatively travelling component waves in each of the two sections of duct. Each spectral component of the pair of time histories in the inlet duct can be described by

$$P_1(\omega) = p_I^+ \exp(-\mathrm{i}\beta_I^+ x_1) + p_I^- \exp(\mathrm{i}\beta_1^- x_1), \tag{A1a}$$

$$P_2(\omega) = p_I^+ \exp(-\mathrm{i}\beta_I^+ x_2) + p_I^- \exp(\mathrm{i}\beta_1^- x_2), \tag{A1b}$$

and in the outlet by

$$P_3(\omega) = p_0^+ \exp(-\mathrm{i}\beta_2^+ x_3) + p_0^- \exp(\mathrm{i}\beta_2^- x_3), \tag{A1c}$$

$$P_4(\omega) = p_0^+ \exp(-\mathrm{i}\beta_2^+ x_4) + p_0^- \exp(\mathrm{i}\beta_2^- x_4), \tag{A1d}$$

where β_1 and β_2 are the complex wavenumbers in the inlet and outlet pipes, respectively, and are defined by

$$\beta = k + \alpha(1 - \mathrm{i}), \qquad \beta^+ = \beta/(1 + M), \qquad \beta^- = \beta/(1 - M), \tag{A2a–c}$$

$$\alpha = (1/ac)(v\omega/2)^{0.5}[1 + (\gamma - 1)Pr^{-0.5}], \tag{A3}$$

where M is the Mach number, α is the viscothermal wave attenuation coefficient, v is the kinematic visosity, γ is the ratio of specific heats and Pr is the Prandtl number, all evaluated at the local flow temperature and gas composition in each relevant section of pipe.

Equations (A1a,b) can be solved directly at each frequency for the component wave amplitudes $p_I^{\pm}$ in the pipe attached to the silencer inlet port and equations (A1c,d) for the amplitudes $p_0^{\pm}$ in the pipe attached at the outlet port, since $\beta_1^{\pm}$ and $\beta_2^{\pm}$ with the associated exponentials are then all constant factors. It is important to note that there is a transport time delay across the system element between planes I and O in Figure A1. This can be taken into account by acquiring and digitizing all four pressure–time histories P_1–P_4 simultaneously. Choosing P_1 as a reference, one can replace the spectral components $p_n(\omega)$ in equations (A1) by the corresponding resulting cross-spectra $S_n(\omega)$, given by

$$S_n(\omega) = \mathrm{E}[P_1^*(\omega)P_n(\omega)], \qquad n = 1, 4, \tag{A4}$$

where $P_1^*(\omega)$ and $P_n(\omega)$ are the windowed and averaged FFT's of the corresponding time histories, and the asterisk represents the complex conjugate. When one includes the corresponding substitutions on the right side of equations (A1), one has, for the corresponding equation (A5a), in place of A1a,

$$S_1(\omega) = P_1^*(\omega)P_I^+(\omega)\exp(-\mathrm{i}\beta_1^+ x_1) + P_1^*(\omega)P_I^-(\omega)\exp(\mathrm{i}\beta_1^- x_1) \tag{A5a}$$

with similar expressions for equations (A5b), (A5c) and (A5d). Equations (A5a) and (A5b) can be solved to yield the corresponding values of $P_1^*P_I^\pm$ in the inlet pipe and equations (A5c) and (A5d) for the values of $P_1^*P_0^\pm$ in the outlet pipe. One notes that the factors $P_1^*(\omega)$ are constant at each frequency and will cancel when the corresponding ratios expressing acoustic performance in equations (14)–(16) are evaluated.

An alternative form of solution [5] is accomplished by expresing equations (A5) in matrix form. Careful comparisons [13] between the results of the two methods applied to sets of experimental data showed that the algebraic solutions described here seemed to give somewhat more realistic results at frequencies close to the pipe and chamber resonances. Otherwise, as one might expect, the results were closely similar. The measured transfer spectra obtained by both solutions were also clearly unrealistic at frequencies when the spacing between the transducer approached an integer multiple of half wavelength. The reason for this is well understood and widely recognized [12].

There are some obvious precautions necessary if reliable measurements are to be achieved. Firstly, in the formulation just presented it has been assumed that all four transducers and signal channels have identical performance, which is unlikely to be true. Therefore, a further cross-calibration to account for any such differences should be included in the signal processing. When all four transducers are exposed to the same acoustic field one again chooses one as a reference and then evaluates the cross-spectral densities with the products $p_1^*p_n$ of the corresponding measured time histories, according to the scheme in equation (A4). The corresponding correction factors would then be $G_{1n} = (p_1^*p_n)/(p_1^*p_1)$, $n = 1, 4$. The corrected spectra that are substituted into equation (A5a) are then given by $S_n(\omega)/G_{1n}$, $n = 1, 4$, upon noting that $S_1(\omega)/G_{11} = 1$. With the alternative matrix approach, one notes [13] that the appropriate correction factors below the leading diagonal of the correction matrix are the complex conjugates of those in corresponding positions above it, a point not clarified in reference [5].

Second, with white noise excitation appropriate procedures are required for the data capture and processing. The sampling rate for digitization must be sufficiently high to avoid aliasing. Furthermore, contamination by noise can be minimized by appropriate low-pass filtering of the signals representing the time histories, before they are digitized. Similarly, the sample records should be long enough to provide sufficient samples to obtain a high number of averages and thus yields adequately smooth spectra. For most of the measured spectra reported here, the sampling rate was 8192 samples per second and data was acquired simultaneously on each channel for sixty seconds. The data was processed by using a 4096-point FFT, Hanning windowed with a 15% overlap. This gave 69 averages and quite smooth results. A lower sampling rate and shorter data length yielding 17 averages was used for Figure 4(a), which then provides a comparison of the extent of smoothing achieved by a fourfold increase in the number of averages.

APPENDIX B: PERFORATE IMPEDANCE MODELS

There is a range of impedance models in the literature that apply to distinctly different situations. The ones of interest here concern perforated tubes enclosed in an expansion chamber. These can be grouped into two classes, which comprise analytic models corrected

by empirical relationships, which have general application, and purely empirical models, which tend to be specific for a given perforate sample. Systematic studies [5] and [6], involving comparisons of an extensive sequence of models representing both classes, showed that the quasi-analytic models described below gave general descriptions of perforate impedance that remained in good agreement with observations.

In accordance with observed behaviour, perforate impedance is normally modelled in two regimes. When, in the absence of grazing flow, the fluctuating velocity amplitude in the holes is less than about two metres a second [1] the perforate impedance exhibits linear behaviour, while at higher velocities this becomes non-linear. Experimental evidence [5] suggests that the limiting velocity just stated increases significantly with grazing flow, and this can be by as much as an order of magnitude when the grazing flow Mach number is 0·2. With grazing flow Mach number $M < 0{\cdot}025$, experimental evidence [1, 5] suggests that the linear regime is maintained as long as the fluctuating pressure amplitude, expressed as a sound pressure level (SPL), remains less than 120–125 dB. This limit also appears to increase both with the excitation frequency and with the grazing flow Mach number. Since the limit depends on the velocity through the holes the porosity σ, defined as the total area of the holes per unit surface area, must also be a factor, which therefore has been included.

With grazing flow Mach number $>0{\cdot}025$, the limiting value of the sound pressure level increases, say, to 135 dB or more as the Mach number increases. For more details of this somewhat complex behaviour, see references [1] and [5]. The measurements reported here were all carried out with white noise excitation at a sound pressure level that was limited to 125 dB by the electrical characteristics of the electret microphones used for these measurements. Thus the perforate impedance models described here are limited to the linear regime, and for consistency were adopted to represent its behaviour in the predictive models.

In the linear regime, with a grazing flow Mach number less than 0·025, the specific resistance including hole end effects and radiation impedance [5] is given by

$$\frac{R_0}{\rho c} = \frac{(8\nu\omega)^{0{\cdot}5}}{\sigma c}\left(1 + \frac{t}{d}\right) + \frac{1}{8\sigma}(kd)^2, \tag{B1a}$$

where t is the plate thickness and d is the hole diameter. The second term on the right side represents the radiation impedance. The corresponding specific reactance is represented by

$$\frac{X_0}{\rho c} = \frac{k}{\sigma}\left[\left(\frac{8\nu}{\omega}\right)^{0{\cdot}5}\left(1 + \frac{t}{d}\right) + t + \delta_0\right], \tag{B1b}$$

where $\delta_0 = 0{\cdot}85d(1 - 0{\cdot}5\sigma^{0{\cdot}5})$. The second factor in the expression for δ_0 represents the influence of hole interference on the effective end correction, while the factor 0·85 represents an approximation to the factor $8/3\pi$ in the analytic expression for the reactance associated with a circular opening in an infinite flange.

With grazing flow $M > 0{\cdot}025$, the specific resistance becomes

$$\frac{R_M}{\rho c} = 0{\cdot}6\,\frac{(1-\sigma^2)}{\sigma}(M - 0{\cdot}025) + \frac{R_0}{\rho c}, \qquad M \leqslant 0{\cdot}05, \tag{B2a}$$

$$\frac{R_M}{\rho c} = 0{\cdot}3\,\frac{(1-\sigma^2)}{\sigma}M + \frac{R_0}{\rho c}, \qquad M > 0{\cdot}05, \tag{B2b}$$

and the corresponding specific reactance is given by

$$\frac{X}{\rho c} = \frac{k}{\sigma}\left[\left(\frac{8\nu}{\omega}\right)^{0\cdot5}\left(1 + \frac{t}{d}\right) + t + \delta\right], \tag{B2c}$$

where $\delta = \delta_0(1 + 305M^3)^{-1}$. The corresponding empirical models for the intermediate and non-linear regimes, which are not of direct interest here, can be found in reference [5]. The survey [6] also showed that the influence of through flow on impedance was significantly smaller than that of grazing flow at the same Mach number. Typically, to minimize static pressure losses, the magnitude of the through flow Mach number is normally significantly less than that of the grazing flow. Thus the influence of flow through the holes on perforate impedance has been assumed negligible for the conditions normally found in the practical silencers of present interest. See for example, the discussion in section 3.4.1 and section 4.1.2.

During the measurements it was found that with porosities exceeding 15–20% of the open area, the perforated tube behaved as if its walls were effectively acoustically transparent, which is a result noted by other observers [14].

APPENDIX C: THE LAYOUT AND DIMENSIONS OF THE TEST SILENCERS

The cross flow silencer no. 1 with triflow silencer no. 1(a) were commercially fabricated from 1·5 mm steel sheet and 50 mm diameter steel tube. They formed part of a sequence supplied for acoustic testing in connection with another project. Details describing their dimensions that were provided by the manufacture were confirmed as closely as possible by measurements on site. They were both 0·5 m long with internal diameter of the outer shell nominally 0·2 m, while that of the pipes was 47 mm. The distance between the pipe centrelines (l_5 in Figure 3(c)) was 50 mm in both. Porous sections were perforated with sets of 3·5 mm diameter holes arranged in staggered rows with circumferential and axial pitch of 5·5 mm in both. This gave them a nominal porosity of 15·9%.

The two internal pipes in silencer no. 1 were perforated over a length of 489·5 mm, labelled l in Figure 3, with unperforated lengths l_1 at the expansion inlet and l_2 at its outlet of 4 and 6·5 mm respectively, while the tailpipe length was 1·01 m overall during the tests. Silencer no. 1(a) had both porous pipes perforated over a length $l = 268$ mm, with $l_1 = l_2 = 12$ mm. The flow reversing chamber at the far end from the inlet was 120 mm long while that at the other was nominally 70 mm long. The ends of the pipes protruded slightly into the chambers so there is some uncertainty concerning some of the precise lengths. The overall length of the tailpipe during testing was either 1·295 or 1·3 m.

The group of silencers no. 2 were all assembled on site using a thick walled aluminium tube of 126 mm internal diameter for the outer case. The perforated pipes were 38 mm internal diameter steel tubes adapted from the set employed during the experiments described in reference [5]. The 1·7 mm thick walls of the two samples used were drilled in two patterns, the outlet pipe with 1·9 mm diameter staggered rows of holes drilled on a 4·55 mm circumferential and axial pitch, while the inlet pipe was drilled with staggered rows of 2·9 mm diameter holes on a 7·45 mm circumferential and a 6·55 mm axial pitch, giving a porosity of 6.8% in both cases. Any drilling rag left on the insides of these pipes had already been carefully removed. The remaining pipework was all plastic pipe of the same internal diameter but with 2 mm thick walls. The baffles supporting the tubes were medium density fibre board 25 mm thick and drilled appropriately to accommodate the perforated tubes and inlet or outlet plastic pipes with centrelines 65 mm apart (l_5 on Figure 3(c)). All gaps were carefully filled with industrial sealant.

With silencer nos. 2 and 2(R), $l = 254$ mm, $l_1 = 84$ mm and $l_2 = 24$ mm with tailpipes 0·874 and 1·017 m respectively.

With silencer nos. 2(c) and 2(d), l, l_1 and l_2 were repeated, while the flow-reversing chambers were 120 mm long, and the tailpipes were respectively 0·973 and 1·43 m. The internal arrangement of the pipes was symmetric and the tailpipe diameter was the same as the others.

With silencers nos. 2(R1) and 2(c1), $l = 210$ mm, $l_1 = 26$ mm and $l_2 = 134$ mm. The tailpipes were 0·915 m long.

Tests were also made with silencers $2(R_2)$ and $2(c_2)$, where the lengths l_1 and l_2 were reversed with tailpipes 1·023 m long; and also with silencers $2(R_3)$ and $2(c_3)$, with $l = 170$ mm, $l_1 = l_2 = 100$ mm, and tailpipe 0·99 m.

The large flow-reversing chamber with attenuation performance plotted in Figure 9 had an internal diameter of 237 mm and a length of 200 mm, with inlet and outlet pipes of 0·51 mm internal diameter with their axes 110 mm apart and a tailpipe 0·798 m long. The small version was of a size similar to silencer series no. 2, since it was made from a section of the thick walled aluminium tube. It was 98 mm long and had 38 mm internal diameter inlet and outlet pipes, and a tailpipe 0·887 long. The six other variants tested had a sequence of inlet or outlet side branches added to the basic chambers, with the large chamber increased in length to 272 m for two of them.